PHYSICAL REVIEW APPLIED **16,** 044030 (2021)

Mapping Charge Recombination and the Effect of Point-Defect Insertion in GaAs Nanowire Heterojunctions

Brian T. Zutter,[1] Hyunseok Kim,[2] William A. Hubbard,[1] Dingkun Ren,[2] Matthew Mecklenburg,[3]
Diana Huffaker,[2,4] and B.C. Regan[1,*]

[1] *Department of Physics & Astronomy and California NanoSystems Institute, University of California, Los Angeles, California 90095, USA*
[2] *Department of Electrical Engineering, University of California, Los Angeles, California 90095, USA*
[3] *Core Center of Excellence in Nano Imaging (CNI), University of Southern California, Los Angeles, California 90089, USA*
[4] *School of Physics and Astronomy, Cardiff University, Cardiff CF24 3AA, United Kingdom*

(Received 9 October 2020; revised 10 August 2021; accepted 26 August 2021; published 18 October 2021)

Electronic devices are extremely sensitive to defects in their constituent semiconductors, but locating electronic point defects in bulk semiconductors has previously been impossible. Here we apply scanning transmission electron microscopy (STEM) electron-beam-induced current (EBIC) imaging to map electronic defects in a GaAs nanowire Schottky diode. Imaging with a nondamaging 80 or 200 kV STEM acceleration potential reveals a minority-carrier diffusion length that decreases near the surface of the hexagonal nanowire, thereby demonstrating that the device's charge collection efficiency (CCE) is limited by surface defects. Imaging with a 300 keV STEM beam introduces vacancy-interstitial (or Frenkel) defects in the GaAs that increase carrier recombination and reduce the CCE of the diode. We create, locate, and characterize a single insertion event, determining that a defect inserted 7 nm from the Schottky interface broadly reduces the CCE by 10% across the entire nanowire device. Variable-energy STEM EBIC imaging thus allows both benign mapping and pinpoint modification of a device's electron-hole-recombination landscape, enabling controlled experiments that illuminate the impact of both extended (one- and two-dimensional) and point (zero-dimensional) defects on semiconductor device performance.

DOI: 10.1103/PhysRevApplied.16.044030

I. INTRODUCTION

Crystal defects in semiconductor devices, whether present at fabrication or introduced later via radiation damage, can dramatically impair device performance [1–6]. Commonly used methods for characterizing semiconductor defects have spatial resolution that is crude compared to the feature size in modern microelectronic devices. For example, capacitance-voltage profiling [7] and deep-level transient spectroscopy [8] can extract defect concentrations and energy levels, respectively, from simple heterojunctions. But the spatial information provided by these techniques is one dimensional at best. Two-dimensional mapping is possible with scanning electron microscope electron-beam-induced current (SEM EBIC) imaging, which can locate electrically active extended (i.e., one- and two-dimensional) defects [3,9–11], monitor the development of conducting filaments in metal-oxide resistive memory [12], measure depletion region widths [13], and map minority carrier diffusion lengths [3,14–16]. However, the spatial resolution of SEM EBIC imaging is limited by the size of its electron-hole (*eh*)-generation volume [17]. In a standard, electron-opaque SEM sample, most primary (beam) electrons deposit nearly all of their energy in the sample. The resulting pear-shaped *eh*-generation volumes are of order 100 nm on a side [17,18], which is large compared to feature sizes in many modern devices.

Because a STEM sample is electron transparent, the corresponding *eh*-generation volume is the cylindrical, narrow neck of the SEM *eh*-generation pear [19]. With this much smaller *eh*-generation volume, STEM EBIC imaging has the potential to achieve much higher spatial resolution than SEM EBIC imaging [20–26]. Moreover, the higher beam energies accessible with STEM (usually 60–300 keV versus the 1–30 keV of SEM) span the knock-on threshold in semiconductors, which allows a STEM operator to choose whether or not to introduce knock-on displacements in a semiconductor device *precisely* at the position of the sub-nm^2 STEM beam. The combination of superior spatial resolution and precision modification enables *in situ* STEM EBIC experiments that directly reveal *eh*-recombination

---

[*] regan@physics.ucla.edu

physics in semiconductor nanodevices. In essence, the STEM's focused electron beam serves both as a highly localized source of β-radiation damage, and as an immediate local probe of its effects. This combination allows individual point (i.e., zero-dimensional) defects to be located to within < 1 nm^2.

To produce targets for demonstrating these capabilities, we fabricate heterojunctions in semiconductor nanowires [Fig. 1(a)], which are model systems for elucidating defect physics [5,14–16,27–29]. We put Au contacts on 130-nm-diameter p-type GaAs nanowires (Fig. S1 within the Supplemental Material [30]) with electron-beam lithography, and then briefly anneal the devices [31,32]. At elevated temperatures gallium and arsenic interdiffuse with the gold at the contacts, forming abrupt (< 2 nm) axial Au-GaAs heterojunctions aligned with the (111) GaAs planes [Fig. 1(b)]. Since the growth direction of the GaAs nanowires is along the [111] crystalline direction, these heterojunctions are self-aligned perpendicular to the nanowire axis. Striations in STEM annular dark-field (ADF) images of the GaAs nanowire [Fig. 1(b)] indicate twin boundaries within the zincblende crystal [27].

Connecting a transimpedance amplifier (TIA) to a device (Fig. 1) allows us to generate a STEM EBIC image simultaneously with every STEM ADF image [20,24,25]. The contrast mechanisms generating the two types of images are entirely different, and thus the images provide complementary information. The ADF images [Figs. 1(a) and 1(b)] provide information only about the device's physical structure (e.g., composition and crystal lattice orientation), while the EBIC image [Fig. 1(c)] also reveals the device's electronic structure, in this case the CCE, the size of the space-charge region, and the minority carrier diffusion length.

II. STEM EBIC SPATIAL RESOLUTION

We understand the EBIC signal as being generated as follows. Within some generation volume G surrounding the path of the primary electrons through the sample, the STEM electron beam creates *eh* pairs. The pairs are created by plasmon decay or by secondary electrons resulting from primary electrons [18,19]. The electron-hole pairs then diffuse some distance, parameterized by a diffusion length L, before recombining probabilistically with a hole. Electrons that happen to diffuse to the space-charge region near the Au-GaAs heterojunction can be permanently separated from their holes by the built-in electric field E. The separated charge is collected by the electrodes and constitutes the EBIC. The CCE, which here is the ratio of the EBIC to the rate of *eh*-pair generation, determines what fraction of *eh* pairs are collected. The *eh*-generation rate is relatively insensitive to crystal defects, while the CCE is lowered by recombination centers within the GaAs. Thus, relative changes in CCE due to carrier recombination have a proportional effect on the EBIC. The EBIC also depends on the beam position within the nanowire through three size scales: the radius R of the *eh*-generation volume, the diffusion length L, and the thickness t of the space-charge region (i.e., the region with nonzero E). A single EBIC image can provide information on each of them [33].

Imaging another device with STEM ADF [Fig. 2(a)] and STEM EBIC [Fig. 2(b)] shows how these length scales collectively determine the shape of the EBIC profile

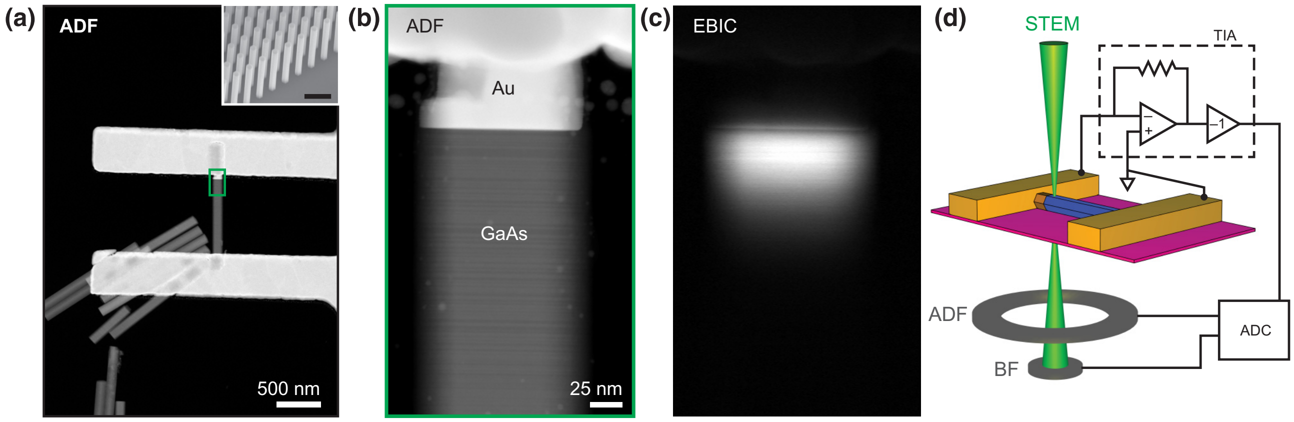

FIG. 1. STEM EBIC imaging of a Au-GaAs nanowire heterojunction. A low-magnification, 200 kV STEM annular dark-field (ADF) image (a) of a device shows 130 nm diameter GaAs nanowires and 250-nm-thick, lithographically defined gold contacts supported by a 15-nm-thick silicon nitride membrane. A SEM image [inset in (a)] acquired with 30° stage tilt shows the nanowires as grown, before transfer to the silicon nitride membrane (unlabeled scale bar is 500 nm). When the region indicated in green in (a) is imaged at higher magnification (b), twin boundaries in the GaAs appear as horizontal lines separated by a few nanometers [Figs. 5(a)–5(e) show such boundaries more clearly in another device]. An EBIC image (c), acquired simultaneously with (b), reveals the *eh* separation that occurs near the Au-GaAs heterojunction. The electrical connections and the locations of the TIA, STEM detectors (ADF, BF), and analog-to-digital converter (ADC) are indicated in a sketch (d).

[Fig. 2(c)]. The STEM ADF image shows the location of the heterojunction, twin boundaries in the GaAs, and some voiding in the Au. The STEM EBIC image shows a CCE that varies in a nontrivial way as a function of position. Just as the point-spread function limits the resolution of *e*-beam lithography [34], the size of the *eh*-generation volume, G, limits the EBIC electronic spatial resolution. It manifests itself clearly here in at least two ways [35]. First, a nonzero EBIC is generated when the beam is incident on the Au side of the heterojunction, even though *eh* pairs are not separated in the Au bulk. Fitting an EBIC line profile along the nanowire centerline on the Au side of the heterojunction [Fig. 2(c), blue profile, purple line] to an exponential $I \propto e^{x/R_{\rm Au}}$ yields a decay length $R_{\rm Au} = 9.4 \pm 0.2$ nm, where the error bar reflects the statistical uncertainty in a linear least-squares fit. This length scale $R_{\rm Au}$ measures how far from the heterojunction the beam can be and still create *eh* pairs that get separated. (While labeled as the radius R of G within the Au, this variable might be better labeled $L_{\rm Au}$ instead, depending on whether the EBIC is primarily generated by secondaries that produce *eh* pairs in the GaAs, or by *eh* pairs in the Au that diffuse to the heterojunction [36].) Second, the EBIC profile maximum 20 nm away from the heterojunction interface indicates that, when the beam is in the GaAs near the heterojunction, some of the G is in the Au, where the CCE is much smaller. Fitting an EBIC line profile along the nanowire centerline on the GaAs side of the heterojunction [Fig. 2(c), blue profile, brown line] to an exponential $I \propto e^{x/R_{\rm GaAs}}$ yields $R_{\rm GaAs} = 9.6 \pm 0.4$ nm, which indicates the radius R of G within the GaAs. This model also explains the hiccup in the line profiles [also clearly visible in Fig. 2(b)] at the heterojunction: moving across the boundary into the Au actually increases the EBIC (even though *eh* pairs are not separated in the Au bulk) because G is continuous while the absolute number of secondary electrons increases discontinuously.

On the Au side of the heterojunction the electric field $E = 0$, while on the GaAs side a substantial electric field $E \neq 0$ exists in the space-charge region. Thus, near the heterojunction the CCE is a step function with approximate values of zero within the Au and unity within the GaAs [33], and the EBIC $\propto G \times$ CCE measures G as just described. Far (> 50 nm) from the heterojunction in the GaAs the E field returns to zero, the minority-carrier transport is dominated by diffusion, and the EBIC measures the CCE. With increasing distance from the space-charge region, the EBIC in the GaAs decays exponentially, with a decay length equal to the minority-carrier diffusion length L. Fitting the EBIC current in the center of the nanowire [Fig. 2(c), blue profile] to $I \propto e^{-x/L}$ [18], where x is the distance from the heterojunction, gives $L = 19.7 \pm 0.1$ nm (green line), where the error bar again reflects the statistical uncertainty in a linear least-squares fit. This relatively short diffusion length likely results not from the nanowire's dense zincblende twin boundaries [Fig. 2(a)], but rather from surface recombination [15]. For instance, the surface-to-volume ratio at the thin edge of the nanowire is larger, and an EBIC profile at the edge [Fig. 2(c), red profile] shows a much smaller minority-carrier diffusion length $L = 13.2 \pm 0.9$ nm (green line). Thus, *eh* pairs generated nearer the nanowire surface are more likely to recombine. While L is much smaller than the nanowire diameter $D = 130$ nm, this fact is not as surprising as it might seem

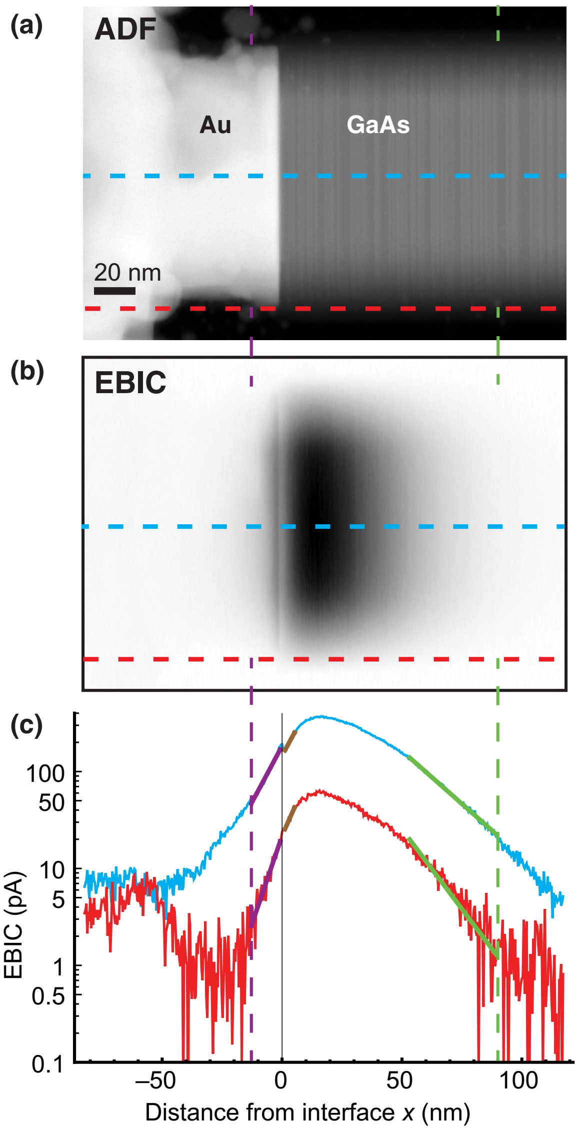

FIG. 2. Mapping *eh* recombination *along* the nanowire. A STEM ADF image (a) and EBIC image (b) are acquired simultaneously with a 200 kV accelerating potential. EBIC line profiles (c) are extracted from the center (dashed blue line) and the edge (dashed red line) of the device in (a),(b). The EBIC decay length in the Au (purple line) and the GaAs (brown line) measures the radius R of the *eh*-generation volume G in each material. In the GaAs far (> 50 nm) from the interface, the EBIC decay length (green line) measures the minority-carrier diffusion length L. All panels are aligned on the same x axis.

at first: on average, any point in a long cylinder of diameter D is only a distance $D/6$ away from the cylinder surface.

The nanowire's simple shape facilitates the interpretation of the EBIC data. ADF STEM data [Fig. 3(a) is equal to Fig. 2(a) rotated] show that the nanowire's cross section [Fig. 3(b)] is a near-perfect hexagon [Fig. 3(c)]. To give a sense of scale, a slice of a cylindrical *eh*-generation volume with $R = 10$ nm is superimposed on the GaAs nanowire's hexagonal cross section in Fig. 3(c).

STEM EBIC imaging's extraordinary spatial resolution reveals how charge recombination varies as a function of not only the nanowire's axial coordinate, but also its radial coordinate (compare, e.g., Ref. [15]). Extending the STEM EBIC analysis of Fig. 2 by fitting at every distinct axial coordinate, we map both the minority-carrier diffusion lengths L (which determine the CCE) and the radii R (which determine G) across the width of the nanowire. The diffusion length L decreases from 20 nm near the center axis of the 130-nm-wide nanowire to 13 nm near the edges [Fig. 3(d), green plot], as expected for recombination occurring primarily at the nanowire surface.

The generation volume G's effective radius R is less than 10 nm in both the Au [Fig. 3(d), purple points] and the GaAs (brown points). Because of voiding in the Au [see Figs. 2(a) and 3(a)], these curves are irregular on one side of the nanowire. Near the nanowire's center the corresponding (cylindrical) STEM EBIC generation volume is $G \sim 4 \times 10^4$ nm^3, while a SEM generation volume with effective radius $r \simeq 100$ nm (appropriate for a 5 keV accelerating voltage [17]) is 100 times larger. STEM EBIC's resolution advantage is approximately r/R, or a factor of 10, relative to SEM EBIC.

Taking the "electronic structure resolution" to be the full width at half maximum of the generation volume, our measured resolution is $(2\ln 2)R = 14$ nm. Note that our STEM EBIC images show smaller features, implying better STEM EBIC resolution, but that these features are primarily generated by changes in physical structure, not electronic structure. For instance, the STEM EBIC images show both the thickness variations that accompany the twin boundaries (approximately 2 nm) and the EBIC hiccup (approximately 3 nm) at the heterojunction (Fig. S6 within the Supplemental Material [30]).

This resolution advantage creates qualitatively superior capabilities: STEM EBIC, unlike SEM EBIC, can map device parameters like the minority-carrier diffusion length *across* an individual nanowire. Our measured R_{GaAs} of 10 nm is an order-of-magnitude larger than predicted by the CASINO Monte Carlo simulator [19,37,38]. We attribute this discrepancy to CASINO's omission of plasmon generation (the dominant energy loss mechanism in GaAs for electrons of < 50 eV energy [39]) in its calculation of stopping power at low electron energies.

Within 50 nm of the interface, the EBIC signal is below the continuation of the green lines on the log-linear plot [Fig. 2(c)]. Near the heterojunction we might instead expect the EBIC increase as the local E field increases in the space-charge region. As mentioned above, the

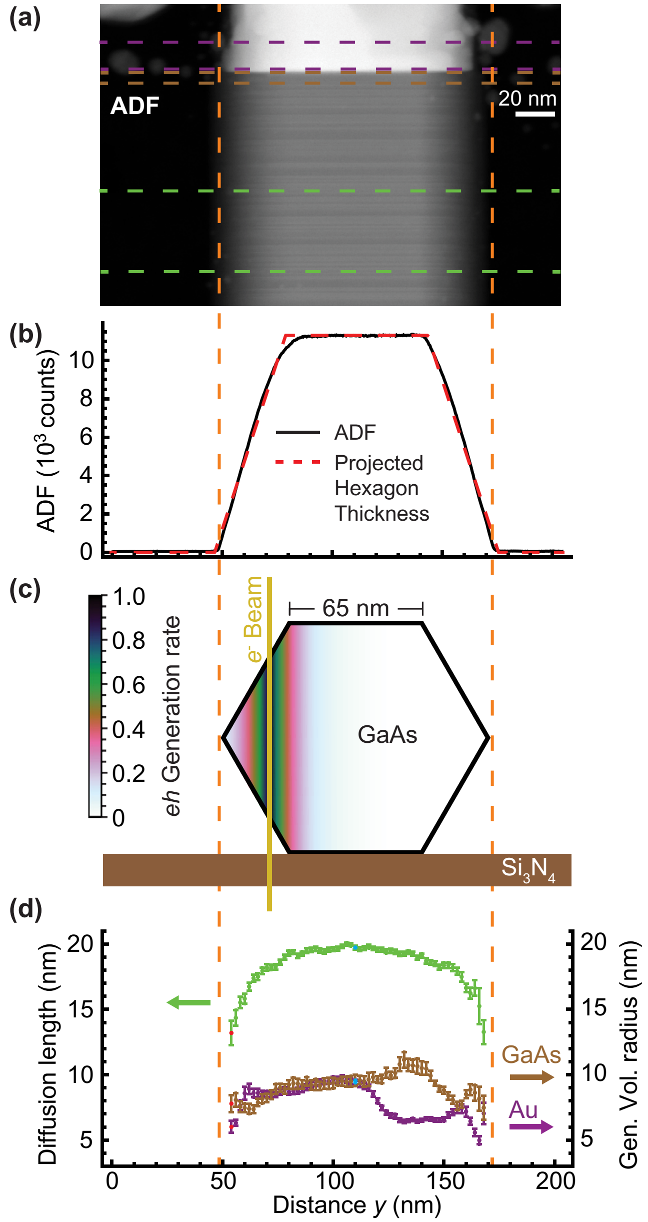

FIG. 3. Mapping *eh* recombination *across* the nanowire. (a) The data of Fig. 2(a) are rotated 90° to align the Schottky interface with the horizontal axis. Summing the ADF signal from the dashed green ROI in (a) gives a profile (b) approximately proportional to the sample thickness. This profile agrees well with the projected thickness of a geometrically perfect hexagon [dashed red line in (b)]. A slice of the cylindrical *eh*-generation volume is overlaid on the nanowire cross section (c), with a decay radius $R = 10$ nm. The generation volume radii R in Au and GaAs and the minority-carrier diffusion length L in the GaAs are plotted as a function of radial position across the hexagonal nanowire in (d). The L and R measurements shown explicitly in Fig. 2(d) are highlighted in blue (center) and red (edge) here. All panels are aligned horizontally on the same distance axis.

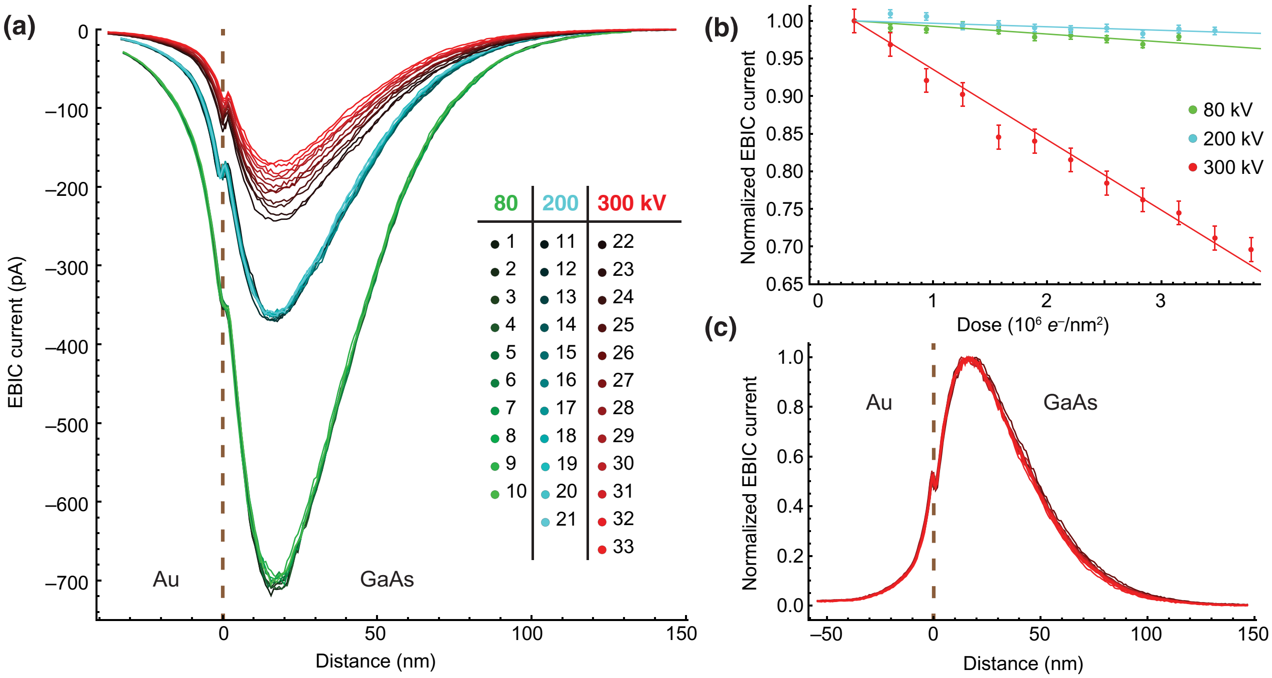

FIG. 4. STEM EBIC at 80, 200, and 300 kV accelerating voltage. Line profiles (a) show the effect of repeated imaging of a device (shown in Fig. 5) at 80 (green), 200 (cyan), and 300 kV (red). Line profiles are extracted from the cyan boxes shown in Fig. 5(a). Only the 300 kV curves show a significant decrease in the EBIC with repeated imaging. Plotting the profile minima, normalized relative to their initial values, versus dose shows (b) a linear dose effect at 300 kV and insignificant effects at 80 and 200 kV. At 300 kV the maximum EBIC decreases by approximately 3% per image. Error bars on the 80, 200, and 300 kV data series are determined by setting the reduced $\chi^2 = 1$ for the linear fits. Normalizing the profiles of the 300 kV data series by the minimum value of each (c) shows that only the amplitude of the EBIC line profile changes, not the shape.

observed decrease indicates that some of the *eh*-generation volume G is in the Au [Fig. 3(d)]. Based on the position of the knee in the EBIC data, the thickness t of the space-charge region is approximately 50 nm.

III. MAPPING THE ELECTRONIC IMPACT OF POINT DEFECTS

To compare damage rates at various accelerating voltages, we image the device of Figs. 2 and 3 while keeping all other imaging conditions (e.g., the 50 pA STEM beam current, 762 μs pixel dwell time, and 0.87 nm pixel size) constant (Fig. 4). Repeated imaging at 80 and 200 kV has little effect on the EBIC, but 300 kV imaging markedly reduces the EBIC signal [Fig. 4(a)]. (The EBIC magnitude decreases as the accelerating potential increases because higher energy electrons deposit less energy per distance traveled in a solid [40].)

As a function of dose, the EBIC, and thus the CCE, decreases linearly at 300 kV [Fig. 4(b)]. We attribute the reduction in CCE to knock-on damage that introduces electronically active vacancy-interstitial (V-I) defects, probably on the As sublattice [41]. These defects function as *eh*-recombination centers, reducing the current that is collected to form the EBIC signal. Energy and momentum conservation dictate that the maximum possible energy transfer from a beam electron to a gallium (mass number $A = 70$) nucleus is 2.7, 7.5, and 12.2 eV for incident electron kinetic energies of 80, 200, and 300 keV, respectively [40]. The maximum energy transfer varies inversely with the mass of the target nucleus, so the numbers for arsenic ($A = 75$) are nearly the same (2.5, 7.0, and 11.4 eV, respectively). Gold ($A = 197$) allows only $70/197 \sim 1/3$ the energy transfer, which is small enough at all of the accelerating voltages used in these experiments that the displacement or knock-on damage in this material is negligible. But the displacement damage threshold energy in GaAs is approximately 10 eV [1,41–43] (although with substantial uncertainty—see Ref. [43] and the references within), which leads us to expect an onset of electron-beam-induced displacement damage between the accelerating voltages of 200 and 300 kV.

One might expect sputtering to be a more important damage mechanism than displacement, since sputtering has larger cross sections and smaller threshold energies [44]. However, while we expect that sputtering does occur in these experiments, we do not attribute the CCE drop to this mechanism for two reasons. First, sputtering is expected at all three accelerating voltages, but changes in EBIC are insignificant at 80 and 200 kV (Fig. 4).

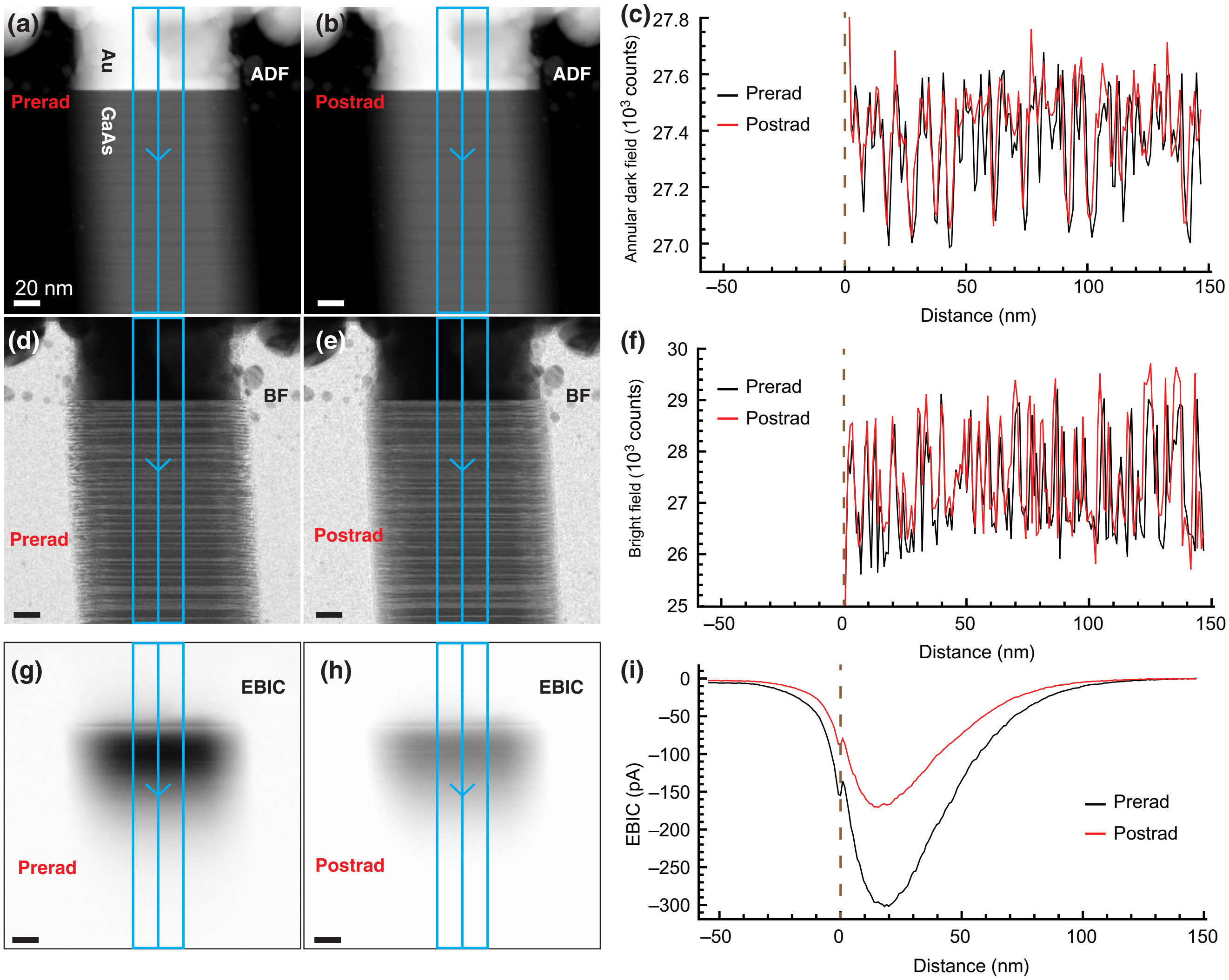

FIG. 5. Annular dark-field, bright-field, and EBIC imaging before and after irradiation with 300 kV STEM electrons. STEM ADF, bright-field (BF), and STEM EBIC images acquired before (a),(d),(g) and after (b),(e),(h) a dose of 6.0×10^6 e^-/nm^2 at 300 kV accelerating voltage. The total dose is applied while acquiring the twelve images No. 22–No. 33 (Fig. 4) and three alignment images (between No. 21 and No. 22). Line profiles are extracted (c),(f),(i) by horizontally averaging data within the blue boxes. A dashed brown line in the line profiles indicates the Au-GaAs interface. Irradiation produces almost no change in the conventional imaging channels (ADF, BF), but a 44% decrease in the maximum EBIC, which highlights the advantage of EBIC over conventional imaging for revealing functional properties such as the CCE.

Second, the EBIC spatial profile is consistent with a surface recombination probability near unity (Figs. 2–3). In short, while sputtering damage doubtless occurs, the nanowire surface is already so defective that further damage has no significant effect on the *eh*-recombination probability.

After they have been normalized relative to their minima, all twelve EBIC profiles acquired at the damaging 300 kV accelerating voltage overlap closely [Fig. 4(c)]. That the defects introduced do not change the minority-carrier diffusion length L indicates that L is still dominated by surface recombination, and that this length scale is determined by the nanowire cross section as discussed earlier.

Repeated imaging of this device at 300 kV thus causes a substantial reduction in the EBIC (and thus the CCE) of the nanowire junction—the radiation damage destroys this device's ability to effectively separate of *eh* pairs. Given the large dose (6×10^6 300 keV electrons per square nanometer) and accompanying efficiency drop, it is remarkable that the device appears undamaged in the standard STEM imaging channels [Figs. 5(a)–5(f)]. But while standard STEM imaging is blind to the inserted defects, which have a relatively minor effect on the nanowire's physical structure, EBIC imaging [Figs. 5(g)–5(i)] vividly reveals their outsize impact on the nanowire's electronic structure (namely a 44% reduction of the maximum EBIC).

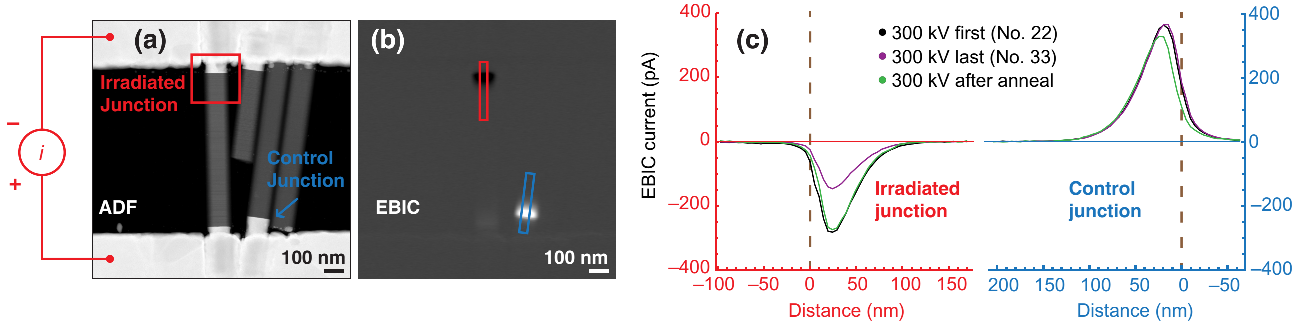

FIG. 6. STEM EBIC before and after annealing. A low-magnification STEM ADF image (a) of the device of Figs. 2–5 shows both the heavily irradiated Au-GaAs heterojunction (red square) and the adjacent control, a heterojunction irradiated less frequently and only at low magnification (cyan arrow). The simultaneously acquired EBIC image (b) shows that the two heterojunctions have EBICs with opposite signs because of their relative orientations in the circuit. The red and cyan rectangles in (b) indicate the sources of the line profiles in the red and cyan plots of (c). After irradiation with 300 kV electrons the magnitude of the irradiated heterojunction's EBIC is reduced relative to the control. After an anneal the irradiated heterojunction's EBIC recovers.

The device of Figs. 2–5 is part of a larger circuit (Fig. 6). At low magnification a second heterojunction, on an adjacent nanowire but also in the circuit, is visible. The second heterojunction is imaged at lower magnification and less frequently (4.8 nm pixel size, 0.762 μs dwell time), and is thus subjected to less than 1% of the radiation dose of the irradiated junction. This adjacent junction can control for changes that are independent of radiation dose.

To corroborate the role of radiation-induced defects in the observed EBIC reduction, after image No. 33 of Figs. 4–5 we anneal the nanowire device in an inert argon atmosphere at 250 °C for 30 min. Such treatment reduces the density of V-I defects within the nanowire, since the elevated temperature makes the beam-induced defects mobile, allowing interstitials and vacancies to meet and annihilate [41,45]. After the annealing treatment, we image the nanowire heterojunction again (Fig. 6). The anneal restores the EBIC to its preirradiated value (i.e., restores the 44% lost) while changing the measured EBIC in the control junction by only a small amount ($< 10\%$). The postanneal restoration is consistent with the hypothesis that the radiation-induced CCE reduction is caused by defects—specifically V-I defects—that anneal away at high temperature.

The STEM's precise electron-beam positioning allows us to observe the effect of selectively dosing just part of the nanowire. In an experiment performed on the Fig. 6 device (after the annealing experiment), we irradiate a narrow strip of GaAs that only spans half of the nanowire heterojunction [denoted by the dashed green box in Fig. 7(a)]. With 300 kV, a 50 pA beam current, a 0.633 nm pixel size, and a 2.3 ms pixel dwell time, the dose per area per strip image, 1.8×10^6 e^-/nm^2, is 5.5 times that of the Fig. 4 experiment. As in the experiment of Fig. 6, we acquire low-dose images before and after the high-dose images for purposes of comparison. (Here a 153 μs dwell time and 1.27 nm pixel size of the two low-dose images contributes only 1.1% of the combined dose from the three strip images.) The difference between the before and after images [Fig. 7(d)] shows that the localized strip irradiation decreases the CCE across the entire width of the nanowire.

By comparing consecutive EBIC images we can, in some cases, precisely identify the position where an electrically active defect is inserted. ADF [Figs. 7(e1)–7(e3)] and EBIC [Figs. 7(f1), 7(f2), 7(d3)] images are collected simultaneously in the three high-dose strip images. In the (standard) raster pattern used here, the electron beam scans across one row from left to right, and then moves down to scan the next rows in sequence in the same direction. Each strip image shows a dose-induced EBIC decrease, as in Fig. 4. EBIC difference images [Figs. 7(g1) and 7(g2)] reveal a sudden drop (8 pA magnitude) in the EBIC that occurs in a single 0.63 nm pixel. We attribute this sudden drop to the insertion of an electrically active defect during the second strip image, at the pixel indicated by the yellow cross [Fig. 7(e2)]. Notably, since the displaced atom of a V-I defect can travel only a few angstroms from its original position at these low energies, and likely in the direction of the electron beam, the yellow cross marks the final location of this single defect [1,43]. Thus, the defect generation volume is much smaller than the eh-generation volume, and EBIC imaging is able to locate V-I insertion events with a much higher precision (< 1 nm) than its electronic resolution of approximately 10 nm.

Comparing in Fig. 7(g1) the 30 pixels to the left and to the right of the insertion event, and the four rows on either side, we find a pre-event EBIC difference of 7 pA and a postevent EBIC difference of 20 pA, with pixel-to-pixel standard deviations of 2.4 pA (Fig. S7 within the Supplemental Material [30]). The approximately 10%, single-pixel reduction in the EBIC is thus statistically significant, and it implies that the inserted defect's recombination cross section σ is approximately 10% of the nanowire's

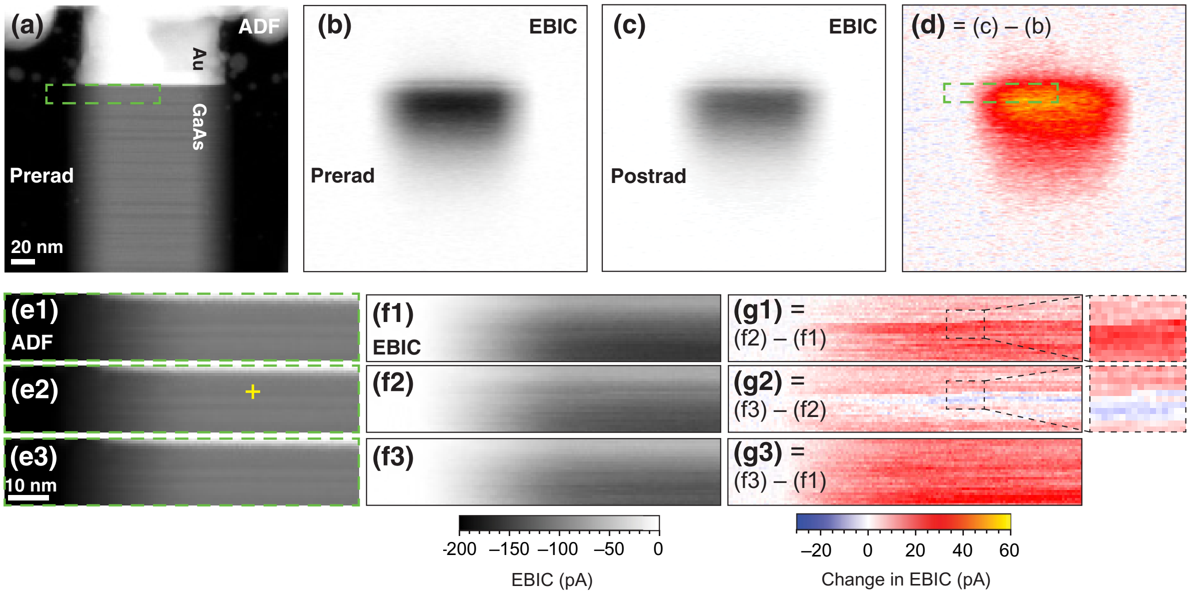

FIG. 7. Defect insertion and pinpoint localization with STEM EBIC at 300 kV. We record the initial state of an Au-GaAs nanowire heterojunction with low-dose (3.0×10^4 e^-/nm^2) ADF STEM (a) and STEM EBIC (b) images acquired simultaneously. We then image the region outlined by the dashed box (a) three times (e1),(e2),(e3) with a high dose (1.8×10^6 e^-/nm^2 per image). After the three strip images we acquire a second low-dose EBIC image (c). A difference image (d) shows that the EBIC decreases across the entire nanowire, even though the dose is confined to a narrow region on the left side of the nanowire. Dark-field strip images (e1),(e2),(e3) show no change during irradiation, while the simultaneously acquired EBIC strip images (f1),(f2),(f3) show significantly smaller signals. EBIC difference images (g1),(g2) reveal a sudden drop in the EBIC magnitude within one 0.63 nm pixel, indicating that a defect is inserted during the second strip image at the location indicated by the yellow cross (e2). Enlarged regions [dashed boxes in (g1) and (g2)] of 11 pixels × 16 pixels (7 nm × 10 nm) demonstrate that both the row and the column of the insertion event can be located precisely. A difference image between the first and third strip images (g3) indicates that, as in (d), the electronic impact of the defect is delocalized. The black-white color scale applies to panels (b),(c),(f), and the blue-yellow color scale applies to panels (d),(g).

10^4 nm^2 physical cross section, i.e., $\sigma \simeq 10^{-11}$ cm^2. This cross section, while large, is within the range of those seen previously [46]. Electron irradiation specifically has been seen to introduce recombination centers with cross sections of this magnitude [47,48].

As with all of the other STEM-beam-induced radiation damage here, this insertion leaves no signature in the conventional ADF imaging. The CCE reduction from this individual defect insertion event is again nonlocal [as in Fig. 7(d)], since the difference between the first and third strip images [Fig. 7(g3)] is uniform.

IV. SUMMARY

In summary, STEM EBIC imaging with an electron-beam acceleration potential of 80 or 200 kV maps the CCE of a GaAs nanowire diode without damaging the device. The minority-carrier diffusion length is found to decrease significantly near the thin edges of the nanowire, and is thus limited by surface recombination. Imaging with the acceleration potential increased to 300 kV introduces defects in the nanowire that decrease the diode's CCE. These V-I defects can be annealed away to restore the original CCE of the diode. Despite being invisible in conventional STEM imaging channels, a V-I defect inserted at 300 kV can be precisely located by identifying an abrupt drop in CCE as the electron beam rasters. As these results show, a modern, variable-energy STEM equipped for EBIC imaging is an experimentally potent combination for producing, locating, and characterizing defects in semiconductor devices with high spatial resolution.

Methods: GaAs nanowires are grown by selective-area epitaxy in a vertical metalorganic chemical vapor deposition reactor (Emcore D-75) at 60 Torr, using hydrogen as a carrier gas. Triethylgallium (TEGa), tertiarybutylarsine (TBAs), and diethylzinc (DEZn) are used as precursors for gallium, arsenic, and zinc p-type dopant, respectively. See the Supplemental Material [30] for complete growth parameters. The GaAs nanowires' measured resistivity is $\lesssim 5\ \Omega \cdot \text{cm}$ (see Fig. S5 within the Supplemental Material and related text [30]), which in bulk GaAs corresponds to a dopant concentration [49] of $\gtrsim 5 \times 10^{15}$ cm^{-3}.

Nanowires are mechanically transferred using a sharp tungsten probe to 15-nm-thick silicon nitride windows reinforced with a 0.8-μm-thick backing layer of silicon oxide (Fig. S2 within the Supplemental Material [30]). Nanowires are located with a SEM, and individual electron-beam lithography patterns are written to each silicon nitride window using polymethylmethacrylate resist. The samples are dipped in 1:10 hydrofluoric acid:water solution for 60 s to remove native GaAs oxides. Immediately afterward, samples are placed in an electron-beam evaporation chamber and 250 nm of gold is deposited. Intruded gold contacts are formed by heating the samples in a rapid thermal annealer at 340 °C for 30 s in a nitrogen atmosphere. To make the sample electron transparent, the silicon oxide support film is removed with a hydrofluoric acid vapor etch. The sample is loaded into a Hummingbird Scientific biasing holder with electrical feedthroughs. STEM images are acquired at 80, 200, and 300 kV accelerating voltage within an FEI Titan STEM. The EBIC signal is measured using a FEMTO DLPCA-200 transimpedance amplifier, set to 10^9 Ω gain with 40 kHz bandwidth. The amplified current signal is fed into an analog input in the STEM, and is synced to the STEM probe position to form an EBIC image.

ACKNOWLEDGMENTS

This work is supported by National Science Foundation (NSF) Grants No. DMR-1611036 and No. DMR-2004897, NSF STC Grant No. DMR-1548924 (STROBE), and Sêr Cymru grants in Advanced Engineering. Data were collected at the Electron Imaging Center for Nanomachines (EICN) at the California NanoSystems Institute (CNSI). Samples were fabricated in the Integrated Systems Nanofabrication Cleanroom (ISNC) at the CNSI. We thank Ting-Yuan Chang for assistance with patterning the nanowire growth template.

[1] Allan Johnston, *Reliability and Radiation Effects in Compound Semiconductors* (World Scientific, Singapore, 2010).

[2] Matthew D. McCluskey and Eugene E. Haller, *Dopants and Defects in Semiconductors* (CRC Press, Taylor & Francis Group, Boca Raton, FL, 2018), 2nd ed.

[3] Ellen Hieckmann, Markus Nacke, Matthias Allardt, Yury Bodrov, Paul Chekhonin, Werner Skrotzki, and Jörg Weber, Comprehensive Characterization of Extended Defects in Semiconductor Materials by a Scanning Electron Microscope, ’ JoVE (Journal of Visualized Experiments), e53872 (2016).

[4] J. R. Srour and J. W. Palko, Displacement damage effects in irradiated semiconductor devices, IEEE Trans. Nuclear Sci. **60**, 1740 (2013).

[5] Fajun Li, Ziyuan Li, Liying Tan, Yanping Zhou, Jing Ma, Mykhaylo Lysevych, Lan Fu, Hark Hoe Tan, and Chennupati Jagadish, Radiation effects on GaAs/AlGaAs core/shell ensemble nanowires and nanowire infrared photodetectors, Nanotechnology **28**, 125702 (2017).

[6] L. C. Hirst, M. K. Yakes, J. H. Warner, M. F. Bennett, K. J. Schmieder, R. J. Walters, and P. P. Jenkins, Intrinsic radiation tolerance of ultra-thin GaAs solar cells, Appl. Phys. Lett. **109**, 033908 (2016).

[7] C. O. Thomas, D. Kahng, and R. C. Manz, Impurity distribution in epitaxial silicon films, J. Electrochem. Soc. **109**, 1055 (1962).

[8] D. V. Lang, Deep–level transient spectroscopy: A new method to characterize traps in semiconductors, J. Appl. Phys. **45**, 3023 (1974).

[9] K. C. Collins, A. M. Armstrong, A. A. Allerman, G. Vizkelethy, S. B. Van Deusen, F. Léonard, and A. A. Talin, Proton irradiation effects on minority carrier diffusion length and defect introduction in homoepitaxial and heteroepitaxial n-GaN, J. Appl. Phys. **122**, 235705 (2017), publisher: American Institute of Physics.

[10] Jeffrey H. Warner, Scott R. Messenger, Robert J. Walters, Geoffrey P. Summers, Manuel J. Romero, and Edward A. Burke, Displacement damage evolution in GaAs following electron, proton and silicon ion irradiation, IEEE Trans. Nuclear Sci. **54**, 1961 (2007), conference Name: IEEE Transactions on Nuclear Science.

[11] Volker Naumann, Dominik Lausch, Angelika Hähnel, Jan Bauer, Otwin Breitenstein, Andreas Graff, Martina Werner, Sina Swatek, Stephan Großer, Jörg Bagdahn, and Christian Hagendorf, Explanation of potential-induced degradation of the shunting type by Na decoration of stacking faults in Si solar cells, Sol. Energy Mater. Sol. Cells **120**, 383 (2014).

[12] Brian D. Hoskins, Gina C. Adam, Evgheni Strelcov, Nikolai Zhitenev, Andrei Kolmakov, Dmitri B. Strukov, and Jabez J. McClelland, Stateful characterization of resistive switching TiO 2 with electron beam induced currents, Nat. Commun. **8**, 1972 (2017), number: 1 Publisher: Nature Publishing Group.

[13] D. Ban, E. H. Sargent, St. J. Dixon-Warren, I. Calder, A. J. SpringThorpe, R. Dworschak, G. Este, and J. K. White, Direct imaging of the depletion region of an InP p–n junction under bias using scanning voltage microscopy, Appl. Phys. Lett. **81**, 5057 (2002).

[14] Christoph Gutsche, Raphael Niepelt, Martin Gnauck, Andrey Lysov, Werner Prost, Carsten Ronning, and Franz-Josef Tegude, Direct determination of minority carrier diffusion lengths at axial GaAs nanowire p–n junctions, Nano. Lett. **12**, 1453 (2012).

[15] Chia-Chi Chang, Chun-Yung Chi, Maoqing Yao, Ningfeng Huang, Chun-Chung Chen, Jesse Theiss, Adam W. Bushmaker, Stephen LaLumondiere, Ting-Wei Yeh, Michelle L. Povinelli, Chongwu Zhou, P. Daniel Dapkus, and Stephen B. Cronin, Electrical and optical characterization of surface passivation in GaAs nanowires, Nano Lett. **12**, 4484 (2012).

[16] Jonathan E. Allen, Eric R. Hemesath, Daniel E. Perea, Jessica L. Lensch-Falk, Z. Y. Li, Feng Yin, Mhairi H. Gass, Peng Wang, Andrew L. Bleloch, Richard E. Palmer, and Lincoln J. Lauhon, High-resolution detection of Au catalyst atoms in Si nanowires, Nat. Nanotechnol. **3**, 168 (2008).

[17] C Donolato, Contrast and resolution of SEM charge–collection images of dislocations: Applied physics letters: Vol 34, No 1, Appl. Phys. Lett. **34**, 80 (1979).

[18] Ludwig Reimer, *Scanning Electron Microscopy : Physics of Image Formation and Microanalysis*, Springer Series in Optical Sciences Vol. 45 (Springer, Berlin, 1998), 2nd ed.

[19] M. Kociak and L. F. Zagonel, Cathodoluminescence in the scanning transmission electron microscope, Ultramicroscopy 70th Birthday of Robert Sinclair and 65th Birthday of

Nestor J. Zaluzec PICO 2017 – Fourth Conference on Frontiers of Aberration Corrected Electron Microscopy, **176**, 112 (2017).

[20] E. R. White, Alexander Kerelsky, William A. Hubbard, Rohan Dhall, Stephen B. Cronin, Matthew Mecklenburg, and B. C. Regan, Imaging interfacial electrical transport in graphene–MoS2 heterostructures with electron-beam-induced-currents, Appl. Phys. Lett. **107**, 223104 (2015).

[21] Jonathan D. Poplawsky, Chen Li, Naba R. Paudel, Wei Guo, Yanfa Yan, and Stephen J. Pennycook, Nanoscale doping profiles within CdTe grain boundaries and at the CdS/CdTe interface revealed by atom probe tomography and STEM EBIC, Sol. Energy Mater. Sol. Cells **150**, 95 (2016).

[22] Myung-Geun Han, Matthew S. J. Marshall, Lijun Wu, Marvin A. Schofield, Toshihiro Aoki, Ray Twesten, Jason Hoffman, Frederick J. Walker, Charles H. Ahn, and Yimei Zhu, Interface-induced nonswitchable domains in ferroelectric thin films, Nat. Commun. **5**, 4693 (2014).

[23] Zoey Warecki, Vladimir Oleshko, Kimberlee Celio, Andrew Armstrong, Andrew Allerman, A. Alec Talin, and John Cumings, Measuring the minority carrier diffusion length in n-GaN using bulk STEM EBIC, Microsc. Microanal. **24**, 1842 (2018).

[24] William A. Hubbard, Matthew Mecklenburg, Ho Leung Chan, and B. C. Regan, STEM Imaging with Beam-Induced Hole and Secondary Electron Currents, Phys. Rev. Appl. **10**, 044066 (2018).

[25] Matthew Mecklenburg, William A. Hubbard, Jared J. Lodico, and B. C. Regan, Electron beam-induced current imaging with two-angstrom resolution, Ultramicroscopy **207**, 112852 (2019).

[26] Aidan P. Conlan, Grigore Moldovan, Lucas Bruas, Eva Monroy, and David Cooper, Electron beam induced current microscopy of silicon p–n junctions in a scanning transmission electron microscope, J. Appl. Phys. **129**, 135701 (2021).

[27] Hannah J. Joyce, Jennifer Wong-Leung, Qiang Gao, H. Hoe Tan, and Chennupati Jagadish, Phase perfection in zinc blende and wurtzite III-V nanowires using basic growth parameters, Nano Lett. **10**, 908 (2010).

[28] Kimberly A. Dick, Claes Thelander, Lars Samuelson, and Philippe Caroff, Crystal phase engineering in single InAs nanowires, Nano Lett. **10**, 3494 (2010).

[29] Daniel Rudolph, Stefan Funk, Markus Döblinger, Stefanie Morkötter, Simon Hertenberger, Lucas Schweickert, Jonathan Becker, Sonja Matich, Max Bichler, Danĉe Spirkoska, Ilaria Zardo, Jonathan J. Finley, Gerhard Abstreiter, and Gregor Koblmüller, Spontaneous alloy composition ordering in GaAs-AlGaAs core–shell nanowires, Nano Lett. **13**, 1522 (2013).

[30] See Supplemental Material at http://link.aps.org/supplemental/10.1103/PhysRevApplied.16.044030 for supplementary Figures S1–S7.

[31] Marta Orrù, Silvia Rubini, and Stefano Roddaro, Formation of axial metal–semiconductor junctions in GaAs nanowires by thermal annealing, Semicond. Sci. Technol. **29**, 054001 (2014).

[32] Vidar T. Fauske, Junghwan Huh, Giorgio Divitini, Dasa L. Dheeraj, A. Mazid Munshi, Caterina Ducati, Helge Weman, Bjørn-Ove Fimland, and Antonius T. J. van Helvoort, In situ heat-induced replacement of GaAs nanowires by Au, Nano Lett. **16**, 3051 (2016).

[33] Melanie Nichterwitz and Thomas Unold, Numerical simulation of cross section electron-beam induced current in thin-film solar-cells for low and high injection conditions, J. Appl. Phys. **114**, 134504 (2013).

[34] Vitor R. Manfrinato, Jianguo Wen, Lihua Zhang, Yujia Yang, Richard G. Hobbs, Bowen Baker, Dong Su, Dmitri Zakharov, Nestor J. Zaluzec, Dean J. Miller, Eric A. Stach, and Karl K. Berggren, Determining the resolution limits of electron-beam lithography: Direct measurement of the point-spread function, Nano Lett. **14**, 4406 (2014).

[35] Brian Zutter, Ph.D. thesis, UCLA 2021.

[36] Jacob B. Khurgin, Fundamental limits of hot carrier injection from metal in nanoplasmonics, Nanophotonics **9**, 453 (2020).

[37] Pierre Hovington, Dominique Drouin, and Raynald Gauvin, CASINO: A new monte carlo code in C language for electron beam interaction –part I: Description of the program, Scanning **19**, 1 (1997).

[38] Dominique Drouin, Alexandre Réal Couture, Dany Joly, Xavier Tastet, Vincent Aimez, and Raynald Gauvin, CASINO V2.42–A fast and easy-to-use modeling tool for scanning electron microscopy and microanalysis users, Scanning **29**, 92 (2007).

[39] A. Rothwarf, Plasmon theory of electron–hole pair production: Efficiency of cathode ray phosphors, J. Appl. Phys. **44**, 752 (1973).

[40] R. F. Egerton, *Electron Energy-Loss Spectroscopy in the Electron Microscope* (Springer, New York, 2011), 3rd ed.

[41] A. Pillukat, K. Karsten, and P. Ehrhart, Point defects and their reactions in e-irradiated GaAs investigated by *x*-ray-diffraction methods, Phys. Rev. B **53**, 7823 (1996).

[42] K. Nordlund, J. Peltola, J. Nord, J. Keinonen, and R. S. Averback, Defect clustering during ion irradiation of GaAs: Insight from molecular dynamics simulations, J. Appl. Phys. **90**, 1710 (2001).

[43] Nanjun Chen, Sean Gray, Efrain Hernandez-Rivera, Danhong Huang, Paul D. LeVan, and Fei Gao, Computational simulation of threshold displacement energies of GaAs, J. Mater. Res. **32**, 1555 (2017).

[44] R. F. Egerton, R. McLeod, F. Wang, and M. Malac, Basic questions related to electron-induced sputtering in the TEM, Ultramicroscopy Proceedings of the International Workshop on Enhanced Data Generated by Electrons **110**, 991 (2010).

[45] L. W. Aukerman and R. D. Graft, Annealing of electron-irradiated GaAs, Phys. Rev. **127**, 1576 (1962).

[46] J. C. Bourgoin, H. J. von Bardeleben, and D. Stiévenard, Native defects in gallium arsenide, J. Appl. Phys. **64**, R65 (1988).

[47] G. M. Martin, A. Mitonneau, and A. Mircea, Electron traps in bulk and epitaxial GaAs crystals, Electron. Lett. **13**, 191 (1977).

[48] D. V. Lang and L. C. Kimerling, in *Lattice Defects in Semiconductors*, Institute of Physics Conference Series No. 23 (Institute of Physics, London, 1974), p. 581.

[49] S. M. Sze and J. C. Irvin, Resistivity, mobility and impurity levels in GaAs, Ge, and Si at 300k, Solid-State Electron. **11**, 599 (1968).